



The Mechanism of Ductility Dip Cracking in Nickel-Chromium Alloys

Subsolidus cracking results from global stresses produced during fusion welding and local stresses generated when coherent or partially coherent second phases form

BY G. A. YOUNG, T. E. CAPOBIANCO, M. A. PENIK, B. W. MORRIS, AND J. J. MCGEE

ABSTRACT. High-chromium (~30 wt-%) nickel-alloy filler metals are desirable for use in nuclear power systems due to their outstanding resistance to corrosion and stress corrosion cracking. However, these alloys are susceptible to welding defects, especially to subsolidus intergranular cracking commonly known as ductility dip cracking (DDC). In order to develop a high-chromium filler metal that is resistant to as-welded defects, a series of Ni-Cr alloys between 16 wt-% and 34 wt-% chromium were assessed for their susceptibility to cracking. Each alloy was evaluated by fabricating a restrained, multipass, automatic gas tungsten arc, V-groove weld, and counting the number of cracks per unit area observable at 50 \times . The type of cracking (subsolidus DDC or solidification cracking) was further differentiated via scanning electron microscopy. The results from these welds, coupled with microstructural characterization, chemical analyses, mechanical testing, microstructural modeling, and finite element modeling indicate that DDC in Ni-Cr alloys is caused by the combination of macroscopic thermal and solidification stresses induced during welding and local grain boundary stresses generated during precipitation of partially coherent (Cr,Fe)₂₃C₆ carbides. Cracking can be mitigated by alloying to minimize (Cr,Fe)₂₃C₆ precipitation (e.g., by Nb and Ti additions), lessening the misfit between the matrix and these precipitates (lowering the Cr and Fe concentration), and by minimizing welding-induced stresses. This mechanism of precipitation-induced cracking (PIC) via misfit stresses is consistent with subsolidus cracking in other alloy

systems including superalloys, nickel-copper alloys, titanium alloys, and ferritic steels where ductility loss corresponds to the time/temperature regime where partially coherent or fully coherent second phases form.

Introduction

Nickel-chromium-iron alloys are used extensively in nuclear power systems for their resistance to general corrosion, localized corrosion, and environmentally assisted cracking. However, concerns with stress corrosion cracking of moderate chromium (14–22 wt-%) alloys such as Alloy 600 and its filler metals (E-182 and EN82) have driven the application of higher chromium (28–30 wt-%) alloys like Alloy 690 (Refs. 1–4). While Alloy 690 and its filler metals show outstanding resistance to environmentally assisted cracking in most water-reactor environments (Refs. 5, 6), these alloys are prone to welding defects, most notably to ductility dip cracking (DDC) (Ref. 4). Ductility dip cracks are intergranular and can be surface connected, which is often an unacceptable condition in components where fatigue, corrosion fatigue, or other forms of environmentally assisted cracking can occur.

Ductility dip cracking is a solid-state phenomenon, typically occurring in reheated weld metal or in base metal heat-affected zones at homologous temperatures between 0.4 and 0.9. The name “ductility dip” comes from the correlation of this cracking to a decrease in ductility, as determined from elevated-temperature tensile testing. This tensile ductility dip has been reported in several alloy systems including austenitic stainless steels (Refs. 7, 8), nickel-based alloys (Refs. 9–17) (including age-hardenable nickel-copper alloys (Refs. 18, 19)), and in both near- α and α + β titanium alloys (Refs. 20–23). In the nickel-chromium alloys of interest, DDC typically manifests itself as intergranular cracks of one grain or less length (Fig. 1) with a minimum in tensile ductility near 870°C (Ref. 24).

While there has been considerable research into DDC (Refs. 8, 11–13, 16, 25), the mechanism or mechanisms responsible for this cracking remain poorly understood (Refs. 7, 8, 12, 13, 16–18, 26–29). Factors suggested to influence DDC have recently been summarized by Collins, Ramirez, and Lippold (Refs. 9, 10, 12, 13) and include grain boundary sliding, second-phase precipitation, impurity element (S, P) segregation, grain boundary character (Ref. 16), degree of grain boundary migration (Refs. 12, 13) and hydrogen embrittlement. The purpose of the present research is to better understand the mechanism of DDC and to develop strategies to mitigate its occurrence.

Experimental Procedure

In order to assess the resistance to DDC and solidification cracking in the Ni-Cr alloy system, welds were made with 24 different filler metals ranging from 15 to 34 wt-% chromium. Complete composi-

KEYWORDS

Alloy 690
Chromium Carbides
Ductility Dip Cracking
EN52
Intergranular Cracking
Nickel-Based Alloys
Subsolidus Cracking
Weldability

G. A. YOUNG, T. E. CAPOBIANCO, M. A. PENIK, B. W. MORRIS, and J. J. MCGEE are with Lockheed Martin Corp., Schenectady, N.Y.

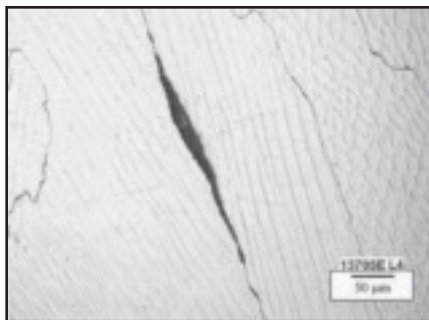


Fig. 1 — Example of a ductility dip crack in a Ni-29Cr-9Fe weld metal (Heat B5). Note that the crack is along the primary (i.e., not migrated crystallographic grain boundary), and is <1 grain in extent (~12 mils or 300 microns).

tions of each weld are detailed in Table 1 and include both commercial alloys (EN62, EN82, and EN52) as well as laboratory fabricated heats of material. The designation “commercial” in the notes column indicates that the material was commercially available. Details of the welding procedure, microstructural characterization, hot ductility testing, and computational analyses are given below.

Weldments

The susceptibility of a given alloy to DDC was assessed by counting the cracks observed in metallographic sections taken from a multipass, V-groove, gas tungsten arc weld with dissimilar metal side rails (carbon steel and 304L stainless steel). This weld is essentially a linear version of a piping safe-end weld common to many nuclear power systems and is shown schematically in Fig. 2. The welding parameters used for this mockup are given in Table 2. Furthermore, the stresses and strains developed in this weld were investigated via finite element modeling.

Microscopy

Each weld was sectioned into nine pieces for crack counts: eight end cut sections perpendicular to the welding direction and one diagonal slice from root to crown of the weld. These nine pieces were metallographically polished to a 0.05-micron finish and examined for defects at 50 \times . Any crack-like observations greater than 75 microns (0.003 in.) in length were recorded and were further examined by higher magnification light optical microscopy and by scanning electron microscopy to differentiate DDC from solidification cracking. This procedure examined approximately 16 square inches of material per weld and the alloys were ranked via the number of cracks per square inch.

The dilution in this weld joint was in-

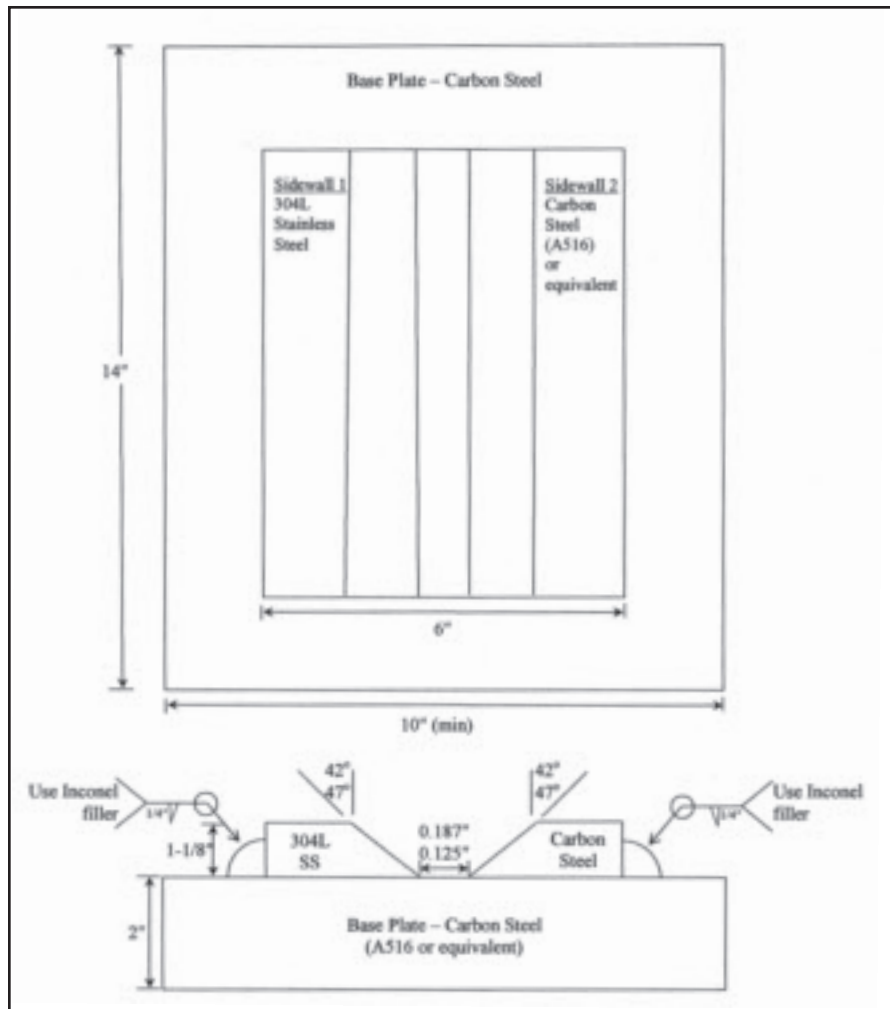


Fig. 2 — Schematic illustration of the V-groove weld used to assess subsolidus cracking (not to scale).

vestigated via scanning electron microscopy and wavelength dispersive spectroscopy (WDS). The iron concentration of a cross section from one weld (Heat A3) was mapped to illustrate the degree of mixing between the iron-based siderail materials and the nickel-alloy weld. The measurements were made on a JEOL 8200 microprobe operated at 15 kV accelerating voltage, with a 90-nA probe current, and at 60-micron step intervals.

Lastly, the grain boundary microstructure from multipass welds of EN82H (Heat A5) and EN52 (Heat B1) were examined via transmission electron microscopy. For this work, grain boundaries in the reheated portion of a weld bead (i.e., in a location that was reheated but not remelted by subsequent weld beads) were first identified via light optical microscopy, and then mechanically sectioned, ground, and electropolished. Care was taken to investigate the reheated portion of the beads since DDC is observed in base metal or weld metal heat-affected zones (Ref. 30). The TEM was performed

on a VG 603 dedicated scanning transmission microscope operated at 300 keV accelerating voltage. Phase identification was determined via selected area diffraction and semiquantitative energy dispersive spectroscopy.

Hot Ductility Testing

Hot ductility testing of EN52 was assessed at both Lockheed Martin and Lehigh University. In both bases, the samples used were standard round bars sectioned from multipass GTAW buildups and the Gleeble testing employed a heating rate of 93°C/s (200°F/s), a cooling rate of 32°C/s (90°F/s), and a stroke rate of 2 in./s. At Lockheed-Martin, 6.3-mm- (0.250-in.-) diameter tensile bars were used to investigate both the on-heating and on-cooling hot ductility in a Gleeble 1500D thermomechanical simulator. At Lehigh, 5-mm- (0.20-in.-) diameter tensile bars were used to confirm the on-cooling hot ductility behavior and to explore the effect of hold time at the ductility mini-

Table 1 — Summary of the Compositions Tested in the V-Groove Weld (wt-%) and Resulting Number of Cracks per Square Inch ^(a)

Heat ID	Notes	Cr	Fe	C	Al	Ti	Nb	Mn	B	Zr	N	S	P	Si	Mg	Cracks/in. ²
A1	1EN62 (commercial)	15.80	6.90	0.030	---	---	2.27	0.83	---	---	---	0.007	0.011	0.17	---	0
A2	Modified EN82 25Cr	25.50	1.25	0.038	0.04	0.01	2.40	2.67	0.0003	<0.01	0.0076	0.0021	0.0015	0.020	0.000015	0
A3	Modifies EN82 27Cr-Fe	27.30	1.14	0.036	0.85	0.25	2.43	2.83	0.0003	<0.01	0.0091	0.001	0.008	0.02	0.001	0
A4	Low C EN82	21.43	2.16	<0.010	0.10	0.37	2.36	1.84	0.0030	---	0.0059	0.001	0.006	---	0.001	0
A5	EN82 (commercial)	19.00	1.34	0.037	0.044	0.30	.02	2.96	0.00008	0.0018	0.0059	0.001	0.006	---	---	0
A6	EN82 (commercial)	19.85	1.05	0.035	0.06	0.27	2.57	3.20	<0.001	<0.001	0.0138	<0.0003	<0.003	0.12	0.008	0
A7	Modified EN82 24Cr	24.05	3.18	0.027	0.03	0.19	2.94	3.05	<0.001	<0.001	0.0182	0.001	0.002	0.15	0.0008	0
A8	Modified EN82 27Cr	26.88	3.00	0.031	0.06	0.19	2.65	3.19	0.0002	0.0002	0.0082	0.0006	0.003	0.15	0.0003	0
B1	EN52 (commercial)	28.91	9.03	0.020	0.67	0.56	<0.01	0.25	<0.001	---	0.0100	<0.001	0.003	0.14	0.004	0.95 ^(b)
B2	Modified EN82 29Cr	29.80	2.91	0.030	0.06	0.19	2.50	3.05	0.0002	<0.001	0.0097	0.0003	0.003	0.14	0.0003	1.00
B3	Modified EN521Nb-1Mn-0.003B-0.003Zr	29.20	9.01	0.023	0.075	0.25	0.94	0.95	0.0026	0.0032	0.0128	0.0011	0.00074	0.16	0.0022	1.70
B4	Modified En521Al-0Ti-3Mn	28.44	9.71	0.050	1.00	<0.01	0.30	2.98	<0.001	<0.01	0.0110	0.005	<0.002	0.014	---	1.70
B5	EN52 (commercial)	29.19	9.03	0.020	0.52	0.57	<0.01	0.24	0.0010	---	---	<0.001	0.008	0.19	---	1.75 ^(b)
B6	Modified EN52 2.5Nb-3Mn	29.30	8.75	0.033	0.70	0.34	2.51	2.97	0.0003	<0.01	0.0110	0.002	<0.002	0.10	<0.002	2.00
B7	A690-like	29.90	9.48	0.014	0.038	0.30	1.70	2.89	0.00012	0.0013	0.0281	0.0039	0.0010	0.210	0.000025	2.90
B8	Modified En82 0Nb	20.18	3.82	0.050	0.09	0.73	0.03	2.38	0.0050	---	0.0048	0.002	0.011	0.37	<0.014	5.40
B9	EN52 with VIM/VARMelting	28.80	8.50	0.038	0.75	0.30	0.027	0.22	0.00042	0.0039	0.0157	0.00056	0.00042	0.110	0.00013	6.85
C1	EN52	28.91	9.07	0.020	0.77	0.28	<0.01	0.16	0.0010	---	0.0098	<0.001	0.004	0.16	<0.01	10.35
C2	EN52	29.21	8.97	0.027	0.68	0.47	<0.01	0.24	0.0003	<0.01	0.0010	0.001	<0.002	0.13	<0.002	13.55
C3	Modified EN52 1.5Nb-2.8 Mn-B-Zr	29.90	9.09	0.019	0.05	0.17	1.46	2.77	0.0040	0.006	0.0136	---	---	---	---	(19.5) ^(c)
C4	Modified EN52 0.9Nb-0.9Mn-B-Zr	28.50	8.87	0.020	0.07	0.25	0.92	0.93	0.0019	0.0096	0.0085	0.00012	0.00012	0.0270	0.00043	(27) ^(c)
D1	Modified EN52 1Al-0Ti	28.82	9.92	0.040	0.98	<0.01	0.02	0.26	<0.001	<0.01	0.0030	0.005	<0.002	0.13	---	>30
D2	Modified EN52 Low Ti	28.91	9.92	0.050	0.74	0.01	0.02	0.27	<0.001	<0.01	0.0150	0.004	<0.002	0.13	---	>30
D3	Modified En52 3Cr	33.28	8.91	0.020	0.60	0.51	<0.01	0.15	0.001	--	0.0022	0.003	<0.002	---	---	>30

(a) The crack counts represent DDC except for heats C3 and C4, which displayed both DDC and solidification cracking.

(b) Heats did not crack if weld joint had similar metal siderails (B1: all Alloy 600, B5: all carbon steel).

(c) Welds contained both DDC and solidification cracks and were excluded from subsequent DDC correlations.

temperature. For the Lehigh tests, a Gleeble HAZ 1000 thermomechanical simulator was used. The peak temperatures for the on-cooling tests were similar, i.e., 1282°C (2340°F) for the Lockheed Martin tests and 1288°C (2350°F) for the Lehigh tests.

Modeling

Three modeling efforts were used to better understand the experiments and interpret the data from the small bead V-groove welds: 1) finite element modeling of the weld joint, 2) Scheil solidification modeling of each composition tested in the V-groove weld, and 3) microstructural modeling of phase stability, phase transformation kinetics, and second-phase misfit.

The finite element modeling was performed via commercially available Sysweld software (Ref. 31). The purpose of this work was to explore the experimental observation that, if the siderail materials in the V-groove weld were identical (e.g., both Alloy 600 or both carbon steel), DDC was suppressed, while dissimilar metal siderails (e.g., one austenitic stainless steel and one carbon steel) promoted DDC. In order to investigate this notion, a simplified two-dimensional finite element model consisting of two siderails and a single weld bead was utilized. The model consisted of three sections corresponding to the left and right siderails and a single weld bead. Linear quadrilateral and triangular elements were used since linear elements are generally better suited for analyses involving plasticity. A single fi-

Table 2 — Summary of Welding Parameters

Process	Pulsed GTAW
Electrode	0.094-in. diameter ceriated tungsten
Shielding Gas	Argon
Preheat	60°F
Interpass Temperature	350°F
Parameters	Primary/Background
Current	200 / 130 A
Voltage	9.5 / 5.0 V
Wirefeed	42 / 30 in./min.
Pulse	0.206 / 0.14 s
AVC Mode	Sample on primary

nite element model with identical thermal and structural boundary conditions was used to investigate the effects of siderail material and filler metal. The model temperature was driven by ramping from

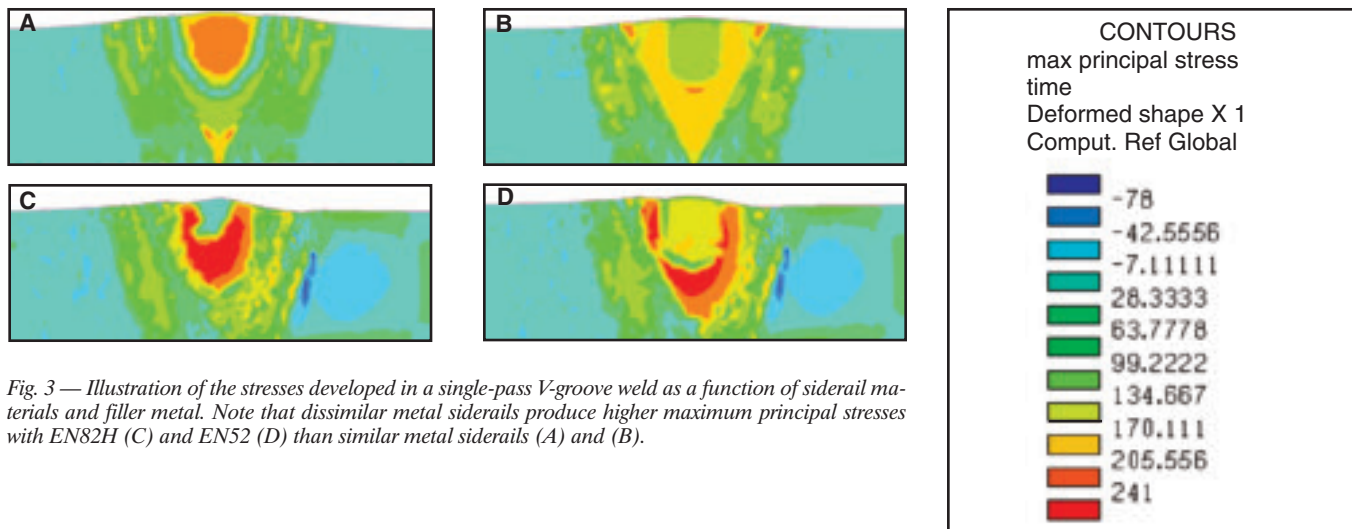


Fig. 3 — Illustration of the stresses developed in a single-pass V-groove weld as a function of siderail materials and filler metal. Note that dissimilar metal siderails produce higher maximum principal stresses with EN82H (C) and EN52 (D) than similar metal siderails (A) and (B).

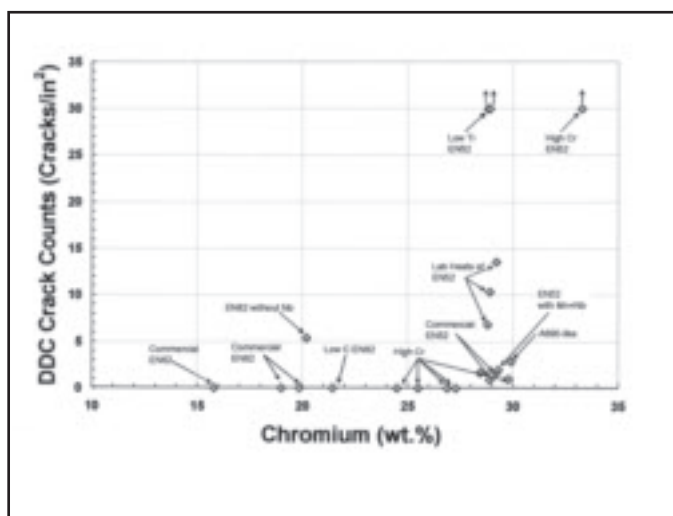


Fig. 4 — Summary of V-groove weld cracking data vs. chromium concentration in the alloy. In general, lower Cr alloys and EN82H-like compositions (i.e., alloys with ~3 wt-% Nb and 3 wt-% Mn) are resistant up to 29 wt-% Cr.

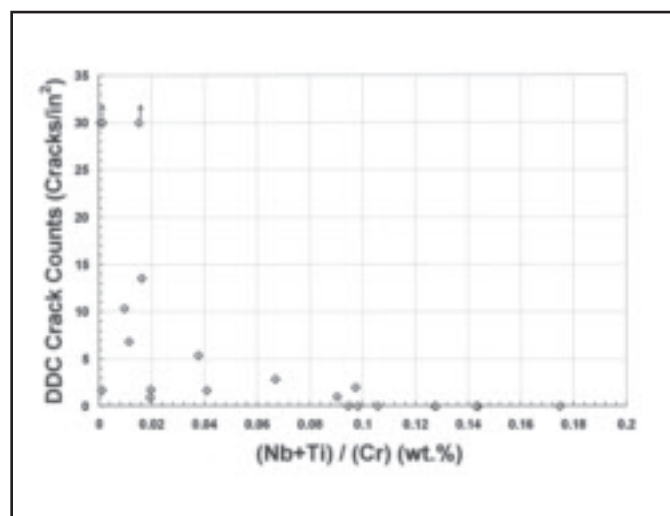


Fig. 5 — Correlation between the number of ductility dip cracks and the ratio of MC-type carbide formers (Nb+Ti) and Cr, which promotes $M_{23}C_6$ -type carbides in high-chromium (> 20 wt-% Cr) nickel alloys.

room temperature to 2912°F (1600°C) in the first second, holding constant for four seconds, and cooling to ambient temperature by convection and radiation. For the stress analysis, the model was constrained horizontally and vertically at the bottom-left siderail, vertically at the bottom-right siderail, and evaluated in the plain strain condition. Loading for the structural analysis is due to thermal expansion and based on the temperature distribution and the interference strain due to phase transformation in the carbon steel end rail. The material combinations investigated were 1) Alloy 600 siderails with EN82 and EN52 filler metals and 2) 304SS and ASTM 516 Grade 70 siderails with EN82 and EN52 filler metals. In all cases, alloy-specific, temperature-dependent material properties were used.

The solidification behavior of each V-groove weld was investigated via *JMatPro*,

version 4.0 software (Ref. 32). This analysis was performed to estimate the amount of carbon in fcc gamma phase at the end of solidification. The calculations utilized the Ni-Fe alloy database and considered the following elements for each alloy (Ni, Al, Cr, Fe, Mn, Nb, Ti, B, C, and N) and the following phases (liquid, fcc nickel, $M_{23}C_6$, M_7C_3 , MC, and Laves phase). Note that *JMatPro* 4.0 utilizes a Scheil-Gulliver solidification model, modified for fast diffusion of carbon and nitrogen (Ref. 33).

The microstructural modeling used both *JMatPro* and *FactSage* (Ref. 34) software. *JMatPro* was used to assess the effect of alloying elements on the precipitation kinetics of $M_{23}C_6$ -type carbides, to generate time-temperature-transformation diagrams for select alloys, and to estimate the misfit between γ' (or γ'') and the matrix of selected nickel-based superalloys. For the TTT calculations, the solvus temperature

for 100% γ was first determined, and curve for 0.1% precipitation of γ' or γ'' calculated. For these calculations, the nominal compositions of the alloys, supplied by the software, were used.

The *FactSage* calculations were performed to assess the effects of temperature, chromium, and iron concentration on chromium-rich carbide stability. These calculations used the SGTE 2004 database, considered the γ , M_7C_3 , and $M_{23}C_6$ phases, and were performed assuming 1 atm of pressure for a temperature range of 1000°–2000°F (538°–1093°C), chromium concentrations between 15 and 35 wt-%, and at two different iron levels (1 and 10 wt-%).

The elastic constants of the $Cr_{23}C_6$ carbide phase were calculated via first-principles methods. To give a sense of the accuracy of this methodology, the elastic constants of nickel were also calculated at

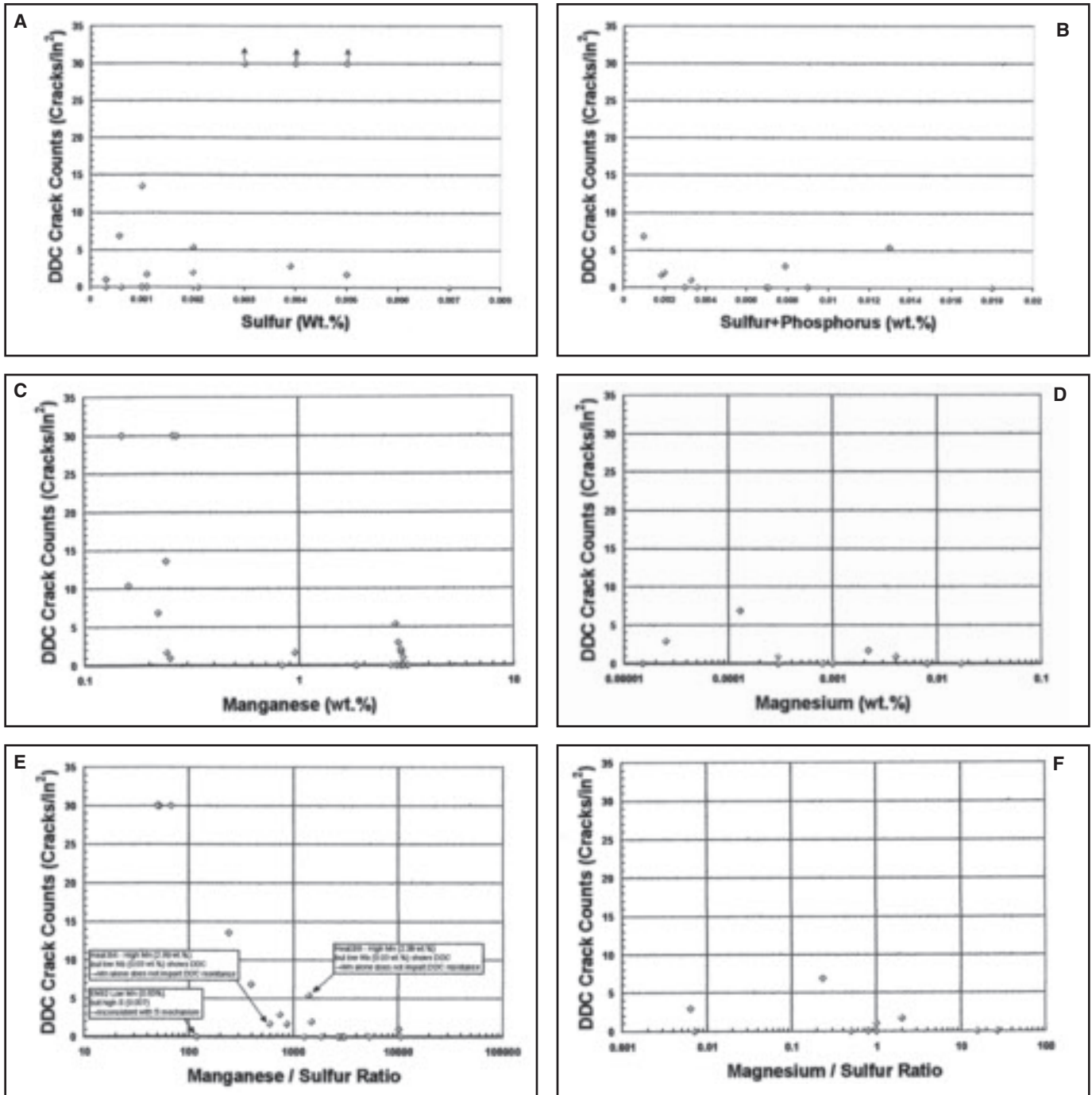


Fig. 6 — Summary of V-groove weld cracking. A — with sulfur; B — with sulfur + phosphorus; C — with manganese; D — with magnesium; E — with manganese/sulfur ratio; F — with magnesium/sulfur ratio. In general, the data show little correlation suggesting little dependence on tramp elements (S and P) as well as sulfide-forming elements (Mg and Mn).

the same level of theory and with identical input parameters. Geometry optimizations and total energies were calculated via density functional theory as implemented in the Vienna Ab Initio Simulation Package (VASP) version 4.6 and the MedeA version 2.1 interface (Ref. 35). The computational procedure for these calculations was to relax the structure to <0.01 eV/angstrom and then calculate the elastic constants

using the MedeA/MT Module. The following parameters were used in the calculations: the Perdew-Burke-Ernzerhof parameterization of the generalized gradient approximation, spin polarized magnetism, a plane-wave cutoff energy of 500 eV, the projector-augmented-wave method, the Ni-pv, Cr-pv, and C pseudopotentials, an $11 \times 11 \times 11$ k-mesh, and three strains (0.001, 0.0025, and 0.005).

Results and Discussion

Results from the V-Groove Weld

Results of the crack counts for the V-groove weld are summarized in Table 1. The data are grouped by the number of cracks per square inch, i.e., A heats showed no cracking, B heats between 0 and 10 cracks/in.², C heats between 10 and 30

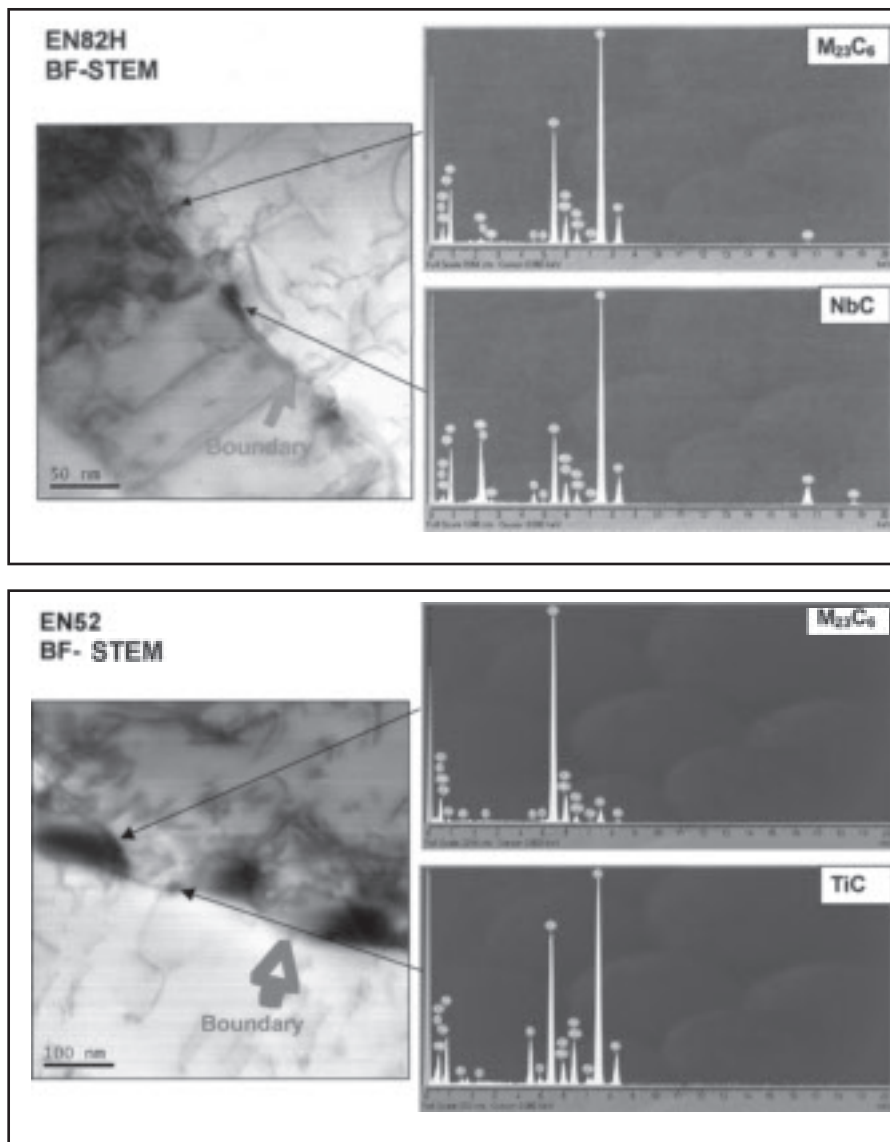


Fig. 7—Representative grain boundary microstructures from multipass welds of EN82H (top) and EN52 (bottom). The EN82H grain boundaries exhibit Nb-rich MC-type carbides with occasional Cr₂₃C₆-type carbides while the EN52 grain boundaries show semicontinuous Cr₂₃C₆-type carbide precipitation and the occasional Ti-rich MC-type carbides.

cracks/in.², and D heats greater than 30 cracks/in.². With the exceptions of Heat B2, where cracking was biased adjacent to the stainless steel siderail, DDC occurred uniformly throughout the weldment. This weld produced repeatable results, i.e., multiple heats of EN82 (A4, A5, A6) did not crack and similar heats of EN52 (B1 and B5) produced the same extent of cracking. Furthermore, this weld differentiates the extent of cracking in the alloys from no cracks in Heats A1–A8, to >30 cracks/in.² in Heats D1–D3. Note that in addition to DDC, hot cracking was observed in two heats of material (C3 and C4), which confounds the crack counts. These heats were not included in subsequent correlations of DDC to composition.

Finite Element Modeling

Finite element modeling helps explain the experimental observation that this V-groove weld geometry with dissimilar metal siderails promotes DDC while the same geometry and welding parameters with similar metal siderails minimizes DDC (see footnote C in Table 1). As shown in Fig. 3, the maximum principal stress developed in the dissimilar metal weld is approximately 5 ksi (35 MPa) higher than the Alloy 600 siderail weld. Also of note is that the stresses developed in EN82 and EN52 in the dissimilar metal weld are comparable [~35 ksi (241 MPa)]. The similar maximum stress developed between DDC-resistant (EN82) and

DDC-prone (EN52) alloys suggests factors other than the macroscopic stress must cause the different DDC resistance between the two alloys.

The Effect of Alloy Composition on DDC

In general, lower chromium alloys such as EN62 and EN82 are immune from DDC in this weld, while higher chromium alloys such as EN52 are susceptible to DDC as shown in Fig. 4. While EN82 did not show DDC in this weld, it is notable that an EN82-like heat without niobium exhibited DDC (Heat B8). Furthermore, EN82-like compositions with typical Nb and Mn levels (~3 wt-%) but higher chromium levels did not DDC, until reaching a level of 29.8 wt-% chromium. Lastly, lowering the titanium of EN52-like heats appears to exacerbate cracking (Heats D1 and D2). Since Nb and Ti are both strong MC-type carbide-forming elements, these observations suggest that carbides may have an important role in DDC. The tendency to form MC-type carbides (vice chromium-rich carbides) is assessed in Fig. 5 which plots the number of ductility dip cracks vs. the (Nb+Ti)/Cr ratio. As shown in Fig. 5, heats with a high (Nb+Ti)/Cr ratio, i.e., a strong tendency to form MC-type carbides vs. Cr-rich carbides, show resistance to DDC.

The occurrence and extent of DDC shows little correlation with bulk levels of tramp elements (S, P) or with sulfide-forming elements (Mn and Mg) as shown in Fig. 6. While sulfur embrittlement of nickel and nickel alloys is well established (Refs. 36–38), it is important to note that very well desulfurized heats (e.g., Heats B8, B9, and C1 with 0.002, 0.00056, and <0.001 wt-% S, respectively) exhibit significant DDC. Additionally, relatively high sulfur heats (e.g., A1 with 0.007 wt-% S) do not DDC in this weld. Furthermore, the DDC data show little correlation with sulfide-forming elements (Fig. 6C and D) or with Mg/S ratio. While there is some trend of decreased DDC with increased Mn/S ratio (6E), the data are cross correlated with Nb as noted on the plot. The few heats with high Mn but low Nb (e.g., B4 and B8) exhibit DDC, discounting a dominant role of MnS formation in DDC resistance. These findings, as well as the different time/temperature dependence for DDC and grain boundary segregation discussed below, indicate that for the alloys tested, sulfur embrittlement is not a primary factor in ductility dip cracking.

Microstructural Findings

As noted previously, one observation from the V-groove weld data is that EN82-like compositions are resistant to DDC (A1–A8) while EN52-like compositions

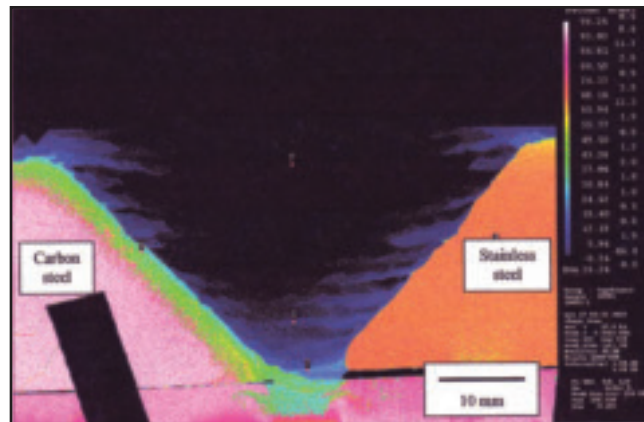


Fig. 8 — Backscatter electron image (top) and quantitative wavelength dispersive spectroscopy compositional map of the iron dilution in the weld. The filler metal was A3 (27.3 wt-% chromium).

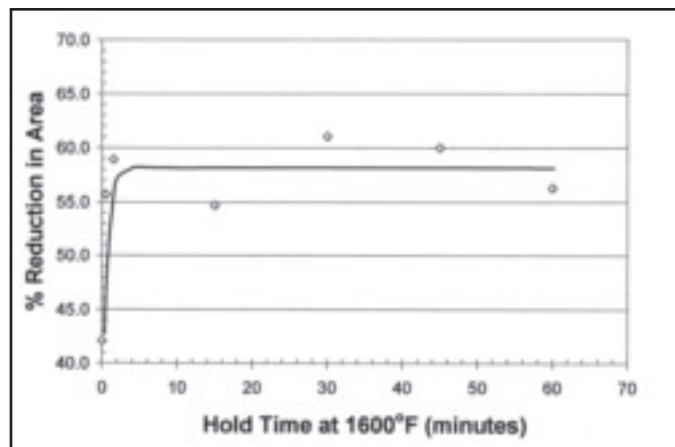
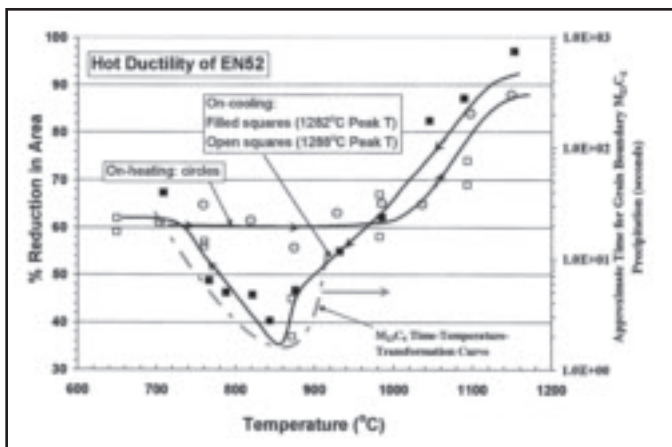


Fig. 9 — The tensile ductility of EN52 filler metal on-heating (circles) and on-cooling (squares). Two heats of material and slightly different peak temperatures 1282°C filled squares and 1288°C open squares) were used for the on-cooling tests. The ductility data are compared to the calculated TTT kinetics of $M_{23}C_6$ carbide precipitation (dashed-dot line), showing very good correlation between the nose of the curve and the ductility minimum near 860°C.

Fig. 10 — Effect of hold time at the temperature of the tensile ductility minimum in EN52, illustrating the transient nature of ductility loss.

(low Nb) are susceptible to DDC. Moreover, DDC in low Ti variants of EN52 show increased cracking susceptibility (e.g., D1 and D2). These observations suggest that these elements, which are known strong MC-type carbide and carbo-nitride formers (where M = Nb, Ti) may play a role in DDC resistance. In fact, the predominant type of carbide is one key difference between EN82, which typically displays a mixture of Nb-rich, MC-type, and $M_{23}C_6$ -type grain boundary carbides and EN52, which forms primarily $(Cr,Fe)_{23}C_6$ -type carbides (with occasional Ti-rich, MC-type carbides) as shown in Fig. 7.

The observation of semicontinuous precipitation of $(Cr,Fe)_{23}C_6$ -type carbides along the grain boundary in a DDC susceptible alloy (EN52) is consistent with the work of Capobianco and Hanson who performed scanning Auger microscopy on in-situ fractured ductility dip cracks and

found extensive $(Cr,Fe)_{23}C_6$ precipitation on the fracture surface (Ref. 11). It is also notable that the carbides are partially-coherent with one side of the grain boundary with a cube-on-cube $((100)_{M_{23}C_6} \parallel (100)_{fcc\ alloy})$ orientation relationship (Refs. 39, 40). Lastly, it is important to note that since $M_{23}C_6$ carbides are stable to high temperatures and their precipitation displays fast kinetics in Ni-30 wt-% Cr alloys, the microstructural observations of this work and the work of Capobianco and Hanson represent a complex thermal history from multipass welds.

A backscatter scanning electron micrograph and the corresponding compositional map of the iron concentration in the weldment is shown in Fig. 8. As expected, there is significant enrichment in iron adjacent to the carbon steel and 304L stainless steel siderail materials. The iron concentration near the root of the weld is on the order of 30 wt-%, while the iron en-

richment adjacent to the siderails is on the order of 15 wt-% and falls off to the filler metal iron concentration in approximately 0.4 in. (10 mm). As discussed previously, while Heat B2 displayed DDC biased toward the stainless steel siderail, ductility dip cracks were observed uniformly throughout the weldment for the bulk of the alloys that were susceptible to DDC. The uniformity of cracking indicates that this weld is a good test for the DDC susceptibility of the filler metal.

Gleeble Hot Ductility Testing

Results of the Gleeble hot ductility testing on EN52 are shown in Fig. 9. Consistent with previous studies on the hot ductility of austenitic alloys, EN52 shows little evidence of ductility loss on-heating but a significant tensile ductility dip on-cooling (Refs. 7, 26, 41). The minimum in ductility as determined by % reduction in

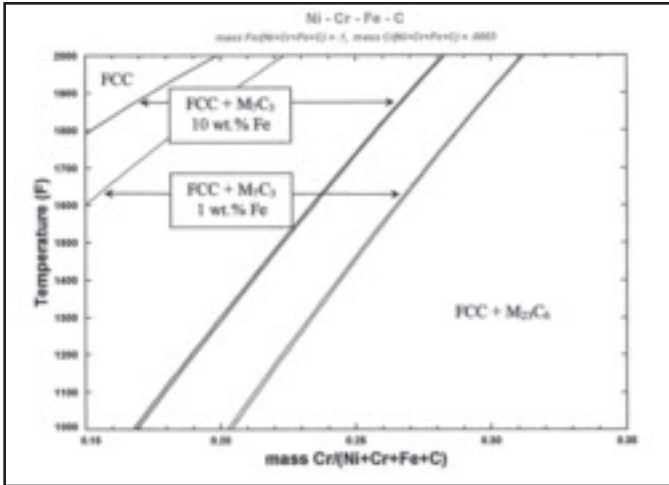


Fig. 11 — Illustration of the effects of chromium and iron on the thermodynamic stability of M_7C_3 and $M_{23}C_6$ -type carbides. Increasing chromium and iron both stabilize the $M_{23}C_6$ phase.

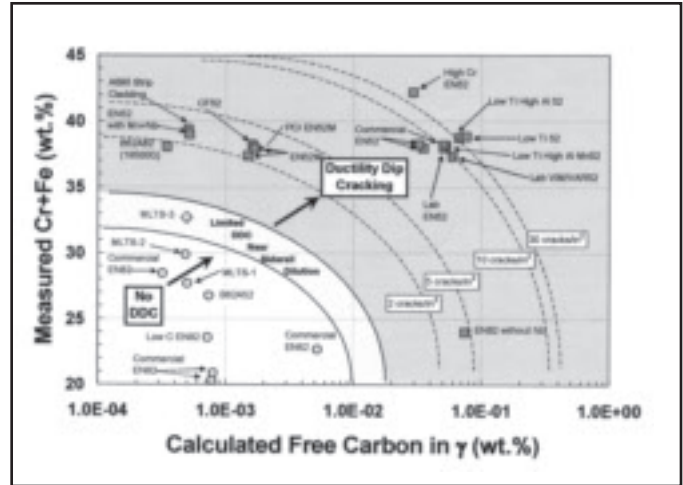


Fig. 12 — Results from the V-groove weld ductility dip crack counts plotted against the measured (Cr+Fe) and calculated free carbon after solidification. Note three distinct regions: DDC free compositions in the lower left, moving up and to the right a transition region where DDC is observed near siderail dilution followed by a region of general susceptibility as (Cr+Fe) and free carbon are increased.

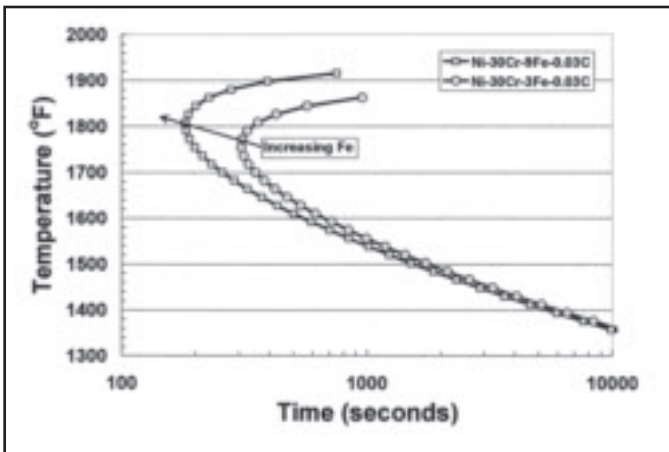


Fig. 13 — Illustration of the effect of iron on the time-temperature-transformation kinetics of $(Cr,Fe)_{23}C_6$ carbides in Ni-30Cr-XFe-0.03 wt-% C alloys. As iron is increased, precipitation is shifted to shorter times, which helps explain the observation of general DDC in heat B6 (8.75 wt-% Fe) but only localized DDC in regions of siderail dilution in Heat B2 (2.91 wt-% Fe). The curves were calculated with JMatPro 4.0 software.

area occurs at approximately 860°C (1580°F). As suggested by Nippes and others (Refs. 7, 17, 41), this ductility minimum corresponds to a temperature regime where second-phase precipitation is occurring. Note the very good correspondence between the minimum in ductility and the nose of the $(Cr,Fe)_{23}C_6$ TTT curve near 860°C. Additionally, the recovery in ductility at temperatures above ~900°C (1652°F) and below ~750°C (1382°F) is also in good agreement with the temperature regime of $(Cr,Fe)_{23}C_6$ carbide precipitation. One implication of increased ductility at temperatures below 750°C is that sulfur embrittlement is un-

likely, i.e., if sulfur is segregating to and embrittling grain boundaries at 1600°F, ductility loss should persist to lower temperatures, in the on-cooling Gleeble testing.

Additional Gleeble testing at the ductility minimum temperature shows that ductility is recovered with hold time at 871°C (1600°F), as illustrated in Fig. 10. The recovery of ductility with hold time at temperature has important mechanistic implications because in this temperature regime (i.e., at homologous temperatures ~0.6–0.7) it would be expected that tramp elements such as sulfur are segregating to the grain boundary and exacerbating embrittlement, not moving away from the grain boundary and improving ductility (Refs. 36, 37, 42, 43).

The Mechanism and Modeling of DDC

The results of the V-groove weld, the TEM study in front of a ductility dip crack, and the Gleeble testing indicate that DDC is associated with the tendency to form grain boundary $(Cr,Fe)_{23}C_6$ -type car-

bides. As shown by the V-groove welds, high levels of Cr tend to promote DDC (Fig. 4), while strong MC-type carbide forming elements such as Nb and Ti impart resistance to DDC — Fig. 5. Furthermore, microstructural investigations reveal semicontinuous $(Cr,Fe)_{23}C_6$ -type carbides in a DDC susceptible alloy (EN52) (Fig. 7) and on DDC fracture surfaces (Ref. 11). Additionally, Gleeble testing shows that regime of ductility loss corresponds to the temperature range of $(Cr,Fe)_{23}C_6$ carbide precipitation (Fig. 9) and that ductility loss recovers with hold time at temperature — Fig. 10. Note that all of the alloys susceptible to DDC will form $M_{23}C_6$ -type carbides in the ductility dip temperature range determined for EN52 (1400°–1800°F) as shown by the thermodynamic stability of the carbides as a function of temperature and bulk chromium concentration in Fig. 11. Notably, lower-chromium, DDC-resistant alloys (e.g., Heat A1, EN62) tend to form pseudo-hexagonal M_7C_3 -type carbides (which are typically incoherent) rather than partially coherent $M_{23}C_6$ -type carbides (Refs. 39, 44, 45).

The tendency of a given alloy to form $M_{23}C_6$ -type carbides can be assessed by plotting the bulk (Cr + Fe) concentration and the calculated free carbon in solution after solidification. The chromium and iron concentrations are summed because Fe can substitute for Cr in the $M_{23}C_6$ carbide. Thermodynamic-based models indicate that approximately 1–2 atomic % of Fe can substitute for Cr in the DDC temperature range of 1400°–1800°F (Ref. 32). The Scheil solidification calculation of the free carbon in the fcc gamma phase integrates the effects of MC-type carbide and

carbo-nitride forming elements (e.g., Ti and Nb).

The correlation of these compositional parameters with the results of the V-groove welds are shown in Fig. 12, which separates the data into three distinct regions: 1) low Cr+Fe and free carbon where the alloys tested are immune to DDC in this weld, 2) a region of increased susceptibility as Cr+Fe and free carbon are increased. In this region, DDC was observed near the stainless steel weld siderail in one heat (B2), possibly due to increased iron and carbon from base metal dilution, and finally 3) a region of general susceptibility to DDC as Cr+Fe and free carbon are further increased. In this regime, DDC occurs uniformly in the weld joint and is not biased by siderail dilution. The dashed lines on Fig. 12 give the approximate extent of DDC, which increases up and to the right (i.e., with increased tendency for $(Cr,Fe)_{23}C_6$ precipitation).

While Fig. 12 provides important insight into interpreting the results of the V-groove weld and offers a practical methodology to develop DDC-resistant alloys, other factors likely affect the tendency for DDC. One notable comparison is between Heats B6 and B2, which have similar compositions with the exception of the iron level (8.75 wt-% in B6 and 2.91 wt-% in B2). Heat B6 with higher iron displayed 2 cracks/in.², throughout the weld, while Heat B2 displayed fewer cracks (1 crack/in.²), that were biased toward the stainless steel siderail dilution area. In the siderail dilution areas, iron and free carbon in the weld metal can be enriched (see Fig. 8 and note that the 304L side contains ~0.02 wt-% C and >65 wt-% Fe), likely increasing the driving force for $(Cr,Fe)_{23}C_6$ precipitation. The effect of increased iron increasing the time-temperature-transformation kinetics of model Ni-30Cr-XFe-0.03C (wt-%) alloys is shown in Fig. 13. Additionally, research on Ni-Cr-Fe ternaries indicates that increasing iron levels will increase the carbide/matrix misfit (Ref. 46), as discussed below.

The correspondence of DDC with the time/temperature regime of the onset of $M_{23}C_6$ precipitation and the noted effect of welding-induced stresses indicates that DDC in Ni-Cr alloys results from the combination of global stresses induced from welding (or imposed via tensile testing) and a local effect associated with precipitation of grain boundary $M_{23}C_6$ -type carbides. One difference between $M_{23}C_6$ and carbides in DDC-resistant alloys is that $M_{23}C_6$ carbides typically nucleate with partial coherency ($(100)_{M_{23}C_6} \parallel (100)_{fcc\ alloy}$), while MC-type and M_7C_3 -type carbides are typically incoherent with the fcc matrix (Refs. 39, 40, 44, 47, 48).

The cube-on-cube orientation rela-

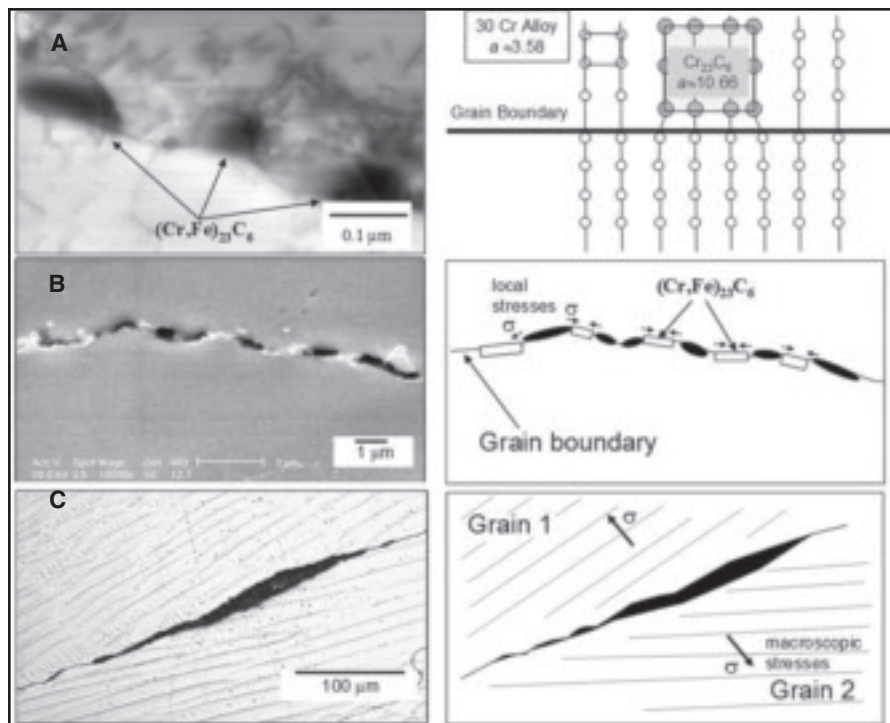


Fig. 14 — Illustration of the mechanism of ductility dip cracking in Ni-Cr alloys. A — Partially coherent grain boundary $M_{23}C_6$ carbides form in reheated weld metal with significant misfit between the carbide and the alloy as shown above and in Fig. 15; B — precipitation generates local grain boundary tensile stresses between carbides promoting crack nucleation; and C — macroscopic stresses generated on-cooling (e.g., thermal and solidification stresses) often link the inter-carbide cracks and result in ductility dip cracking along the crystallographic grain boundary.

Table 3 — Summary of Lattice Parameters and $Cr_{23}C_6$ Carbide/Matrix Misfit for Selected Ni-Cr-Fe Alloys

Material	Lattice Parameter (Angstroms)	d(100) (Angstroms)	$\delta(\%) = \left(\frac{d_{Cr_{23}C_6} - d_{alloy}}{d_{Cr_{23}C_6}} \right) \times 100$	Reference
$Cr_{23}C_6$	10.6595	3.5532	---	(62)
A600	3.553	3.553	0.006	(63)
EN82H	3.570	3.570	-0.473	
A690	3.5757	3.5757	-0.633	

tionship between the carbide and one grain at a grain boundary likely generates appreciable elastic stresses and, in combination with global stresses from welding (or applied during tensile testing), is postulated to result in local intergranular cracking, i.e., ductility dip cracking. Precipitation-induced grain boundary stresses in Ni-30Cr alloys are likely a maximum near the onset of precipitation and decreases with time as: 1) the chromium concentration near the grain boundary is depleted by carbide precipitation and subsequent growth (discussed further below), 2) the carbide/matrix interface grows off the original plane of the grain boundary (i.e., as the precipitation-induced stresses are spatially removed from the grain boundary), and 3) dislocations are generated to help accommodate the interfacial misfit. The mechanism of precipitation-in-

duced cracking is outlined in Figure 14, which shows A — the formation of partially coherent, grain boundary $M_{23}C_6$ carbides and a schematic of the lattice misfit, B — how local tensile stresses develop between carbides and promote crack nucleation, and C — the result of these inter-carbide cracks linking up with subsequent stressing to form a typical ductility dip crack along the crystallographic grain boundary.

The effect of the misfit between $M_{23}C_6$ -type carbides and the matrix can be further assessed by considering the spacing of {100} planes in each phase. The difference between the room-temperature lattice parameters of the $Cr_{23}C_6$ carbide and selected alloys are summarized in Table 3. The room-temperature lattice parameter is a good estimate for the d-spacing in the DDC temperature

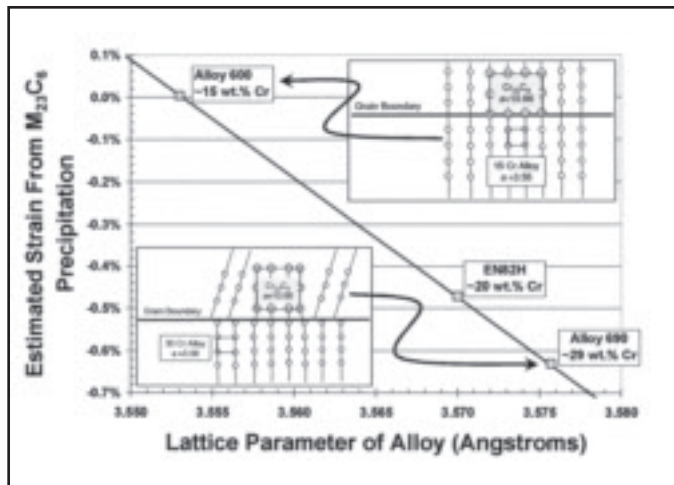


Fig. 15 — Illustration of how the lattice parameter changes in Ni-Cr alloys and the estimated elastic strain with $Cr_{23}C_6$ carbides. The misfit is small for Alloy 600 and increases as chromium is increased. High-chromium weld metal like EN52 should have large misfit similar to Alloy 690.

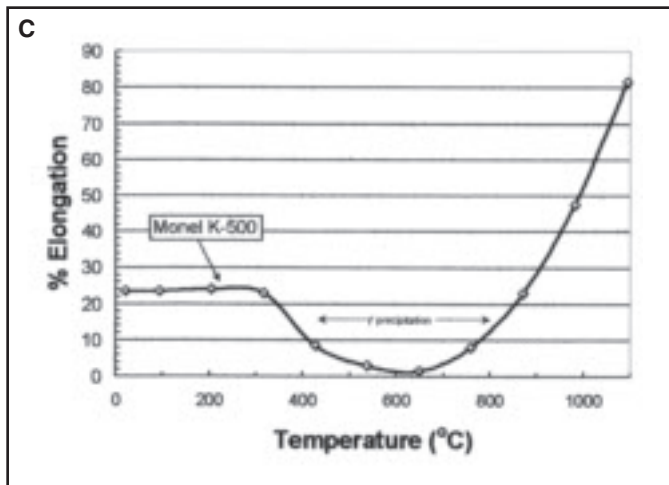
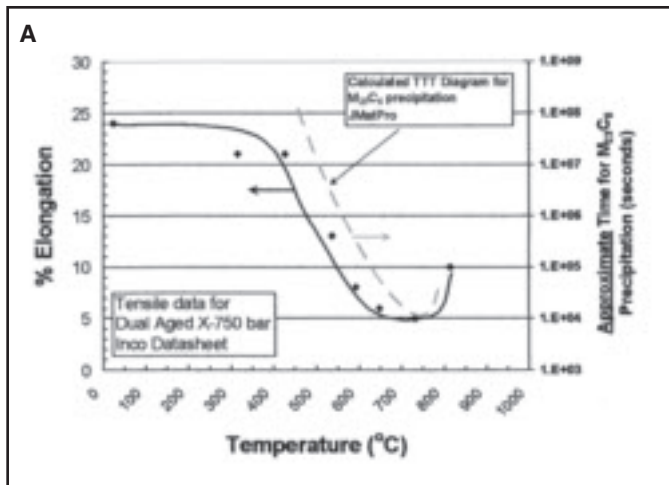
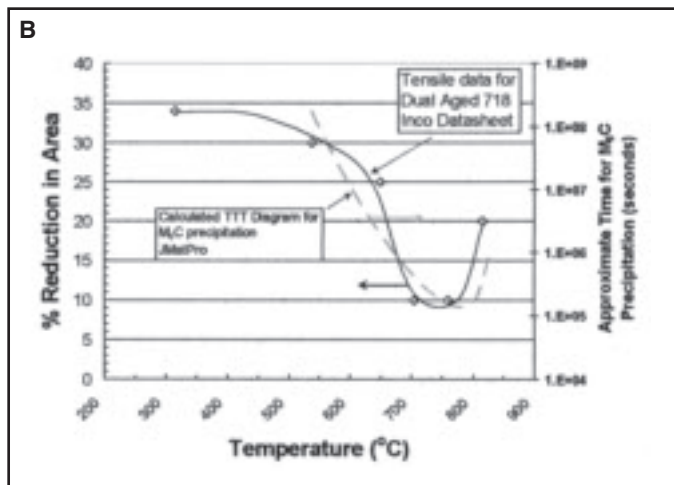


Fig. 16 — Intermediate temperature ductility loss in some other nickel-based alloys. A — Inconel X-750, which occurs in the temperature regime of $M_{23}C_6$ carbide precipitation; B — Inconel 718, which occurs in the temperature regime of M_6C precipitation; C — Monel K-500, which shows large ductility loss in the temperature regime of γ' precipitation.

range (~1400°–1800°F), since the thermal expansion of these both the alloys and $Cr_{23}C_6$ carbides is similar and small in magnitude ($<10^{-5}$ in./in.-°F) (Refs. 5, 49). The misfit strain, δ , was estimated via Equation 1, where d is the (100) interplanar spacing of either the carbide or the alloy.

$$\delta(\%) \approx \left(\frac{d_{Cr_{23}C_6} - d_{alloy}}{d_{Cr_{23}C_6}} \right) * 100 \quad (1)$$

As shown in Fig. 15, the carbide/matrix misfit is a maximum for high chromium (~30 wt-%) alloys and decreases as the chromium content is lowered to ~15 wt-%. For the case of hot-ductility testing performed “on-cooling” from a high solutionizing temperature, this maximum misfit corresponds to short aging times, before grain boundary chromium carbide precipitation can deplete the local

chromium concentration. The change in carbide/matrix misfit as chromium is depleted is consistent with the transient nature of the ductility dip (Fig. 10) and with a precipitation-based mechanism of cracking. Furthermore, the effect of chromium on the carbide/matrix misfit agrees with experimental observations of the known resistance of Alloy 600 to DDC (Refs. 7, 17) and the susceptibility of higher chromium alloys such as EN52 and Alloy 690 (Refs. 11, 24).

In contrast, these observations are inconsistent with the notion that elemental segregation is causal to DDC for the following reasons:

- There is no clear correlation between the bulk sulfur content and the degree of ductility dip cracking — Fig. 6A.
- If grain boundary sulfur segregation was causing or exacerbating intergranular fracture in the DDC temperature range,

the effect should persist on-cooling to lower temperatures, not recover as shown in Fig. 9.

• Since 1400°–1800°F is a temperature regime where sulfur should be segregating to nickel grain boundaries (Refs. 36, 37), the observation of ductility recovery with hold time (Fig. 10) is inconsistent with a segregation based mechanism.

The magnitude of the elastic stress produced in the matrix from nucleation of $M_{23}C_6$ -type was used to assess the stiffness of the carbide since experimental values were not found. The calculations, summarized in Table 4, show reasonable agreement between the experimental and the calculated elastic constants for nickel ($E_{100}^{calculated} = 112$ GPa vs. $E_{100}^{experimental} = 150$ GPa), and the calculations reproduce the correct trend for nickel (increasing stiffness from $\langle 100 \rangle$ to $\langle 110 \rangle$ to $\langle 111 \rangle$). These calculations show that

carbide is significantly stiffer ($E_{100} \sim 334$ GPa) than nickel ($E_{100} \sim 112$ GPa).

The elastic stress produced in the nickel alloy matrix during nucleation can then be estimated from Equation 2, where E , and ϵ are taken as the modulus and the strain in the $\langle 100 \rangle$ direction. This estimation ($E=112$ GPa, $\epsilon = 0.64\%$) results in elastic stresses near 690 MPa (100 ksi), which is far in excess of typical yield strengths for A690 or EN52 [typically in the range of 207–414 MPa (30–60 ksi) at room temperature]. While this is a crude approximation of the actual stresses at the carbide/grain boundary interface, it does show that the elastic misfit stresses are appreciable and could result in cracking, especially when additional global stresses are present as in the case of welding or mechanical testing.

$$\sigma = E \epsilon \quad (2)$$

While misfit strains will partially offset the energy benefit of nucleating with partial coherency on the grain boundary, recent work on Alloy 690 shows that even on high angle grain boundaries, $M_{23}C_6$ -type carbide precipitate with partial coherency (Ref. 47). In other words, the misfit strain between the carbide and matrix is not so large as to negate the benefit of the cube-on-cube precipitation. However, grain boundary misorientation does affect the rate of precipitation as discussed by Lim et al. (Ref. 47). Notably, the misfit between the $M_{23}C_6$ carbide and Alloy 690 quoted by Lim (-0.67%) is similar to the present study (-0.63%).

The effects of coherent precipitate interfacial stresses on second-phase stress, strain, and compositional profiles have been studied in more detail by W. C. Johnson (Ref. 50). Johnson's analyses show that long range stresses can develop from the interface of a coherent second phase and that, using reasonable parameter estimates, the magnitude of the interfacial stress is on the order of ~ 10 – 1000 MPa (1.45–145 ksi). While mainly driven by thermodynamic modeling of phase equilibria, Johnson's work gives further evidence that misfit strains from coherent or partially coherent precipitates can lead to appreciable local stresses and potentially to cracking of the interface.

As shown schematically in Fig. 15, the $\{100\}$ d -spacings of the $Cr_{23}C_6$ carbide are smaller than in high-chromium nickel alloys indicating that the misfit stresses are compressive at the carbide/grain boundary interface. As multiple carbides nucleate along a grain boundary, this causes regions of tension between the carbides and could produce intermittent grain boundary cracks, consistent with some experimental observations of DDC shown in Fig.

Table 4 — Comparison of the Elastic Moduli of Nickel and Chromium Carbide ($Cr_{23}C_6$)

	Elastic Modulus GPa (Msi)			Reference
	$\langle 100 \rangle$	$\langle 100 \rangle$	$\langle 111 \rangle$	
Nickel - Experiment	150 (21.8)	250 (36.2)	320 (46.4)	(64)
Nickel - Calculated	112 (16.3)	196 (28.4)	260 (37.7)	This work
$Cr_{23}C_6$ - Calculated	334 (48.4)	327 (47.4)	325 (47.1)	This Work

Table 5 — Comparison of C-curve Kinetics, Precipitate Mismatch, and Strain Age Cracking Resistance for Selected Superalloys

Alloy	Susceptibility to Strain Age Cracking (Ref. 55)	Calculated Nose of γ' (γ'') Precipitation Curve Time and Temperature (seconds/ $^{\circ}C$ ($^{\circ}F$))(a)	Calculated Mismatch at the Nose of C-curve(%) ^(a)
Inconel 718	Low	197/871 (1600)	+0.44
Inconel X-750	Low	600/832 (1530)	+0.58
Waspaloy	Low	16.9/960 (1760)	+0.11
Rene 41	Medium	8/990 (1814)	-0.28
Udimet 700	High	1.7/1070 (1958)	-0.28
Astroloy	High	1.8/1070 (1958)	-0.39
IN 100	High	0.4/1149 (2100)	-0.45

(a) TTT curves and precipitate mismatch were calculated with *JMatPro* 4.0 software, assuming all phases form and 0.1% fraction transformed.

14. Similarly, failure could also occur at the partially coherent side of the carbide/matrix interface. Of course, the exact ductility dip crack morphology is likely a complex function of a given material's tendency to form $M_{23}C_6$ carbides, local grain boundary orientation, and the magnitude and direction of the global stresses and strains.

Ductility Loss in Other Alloy Systems

The good correspondence between ductility dip cracking in high-chromium nickel alloys and $(Cr,Fe)_{23}C_6$ precipitation, suggests that the same mechanism of precipitation-induced cracking may affect other alloys. Review of nickel-based alloy literature data shows that Alloys X-750, 718, and Monel® K-500 all display significant intermediate temperature ductility dips as shown in Fig. 16 (Refs. 15, 19, 51–53). In the case of X-750, ductility loss corresponds to precipitation of partially coherent $M_{23}C_6$ -type carbide, similar to EN52 and A690. In Alloy 718, the tensile ductility dip correlates to the temperature range of precipitation of M_6C -type carbides. Like $M_{23}C_6$ -type carbides, M_6C have a complex cubic structure, a lattice parameter similar to $M_{23}C_6$ -type carbides (11.26 Å vs. 10.66 Å) and likely have a $(100)_{M_6C} \parallel (100)_{fcc \text{ alloy}}$ orientation relationship with the matrix (Ref. 54). Monel

K-500 exhibits a large ductility dip, both in terms of breadth of temperature range ($\sim 620^{\circ}$ to $1610^{\circ}F$) and ductility loss ($\sim 25\%$ to 2% elongation). The tensile ductility dip corresponds to the temperature regime where γ' will precipitate (Ref. 19), consistent with precipitation-induced cracking. It is also notable that Monel 400, which does not form γ' , does not exhibit this large ductility loss (Ref. 52).

The correspondence of ductility loss with γ' precipitation in Monel K-500 is suggestive of strain-age cracking in nickel-based superalloys (Ref. 55). As shown by Hughes and Berry (Refs. 56, 57), and later by Franklin and Savage (Ref. 58), strain-age cracking occurs in the time/temperature regime of γ' precipitation, analogous to the correspondence of DDC with $M_{23}C_6$ precipitation in EN52-type alloys. Furthermore, studies on the superalloy Rene® 41, show that strain-age cracking is caused by the combined action of global restraint stresses and precipitation-induced stresses (Refs. 59, 60), the same basic mechanism that is postulated for ductility dip cracking. This assertion is supported by the *JMatPro* calculations of misfit strain and precipitation time (Ref. 32), i.e., alloys that are prone to strain-age cracking (e.g., Udimet® 700, IN 100, and Astroloy®) have fast precipitation kinetics and large negative γ/γ' mismatch relative to alloys that are resistant to strain-

age cracking (e.g., Inconel® 718, Inconel® X-750, and Waspaloy®) which display longer times before γ' nucleation occurs and positive mismatch (i.e., matrix compression on precipitation). A summary of precipitation times, temperatures, misfit strains, and tendency to strain-age crack are given in Table 5.

Lastly, it should be noted that the mechanism of precipitation-induced cracking presented herein is very similar to those proposed by Rath et al. for the subsolidus cracking of α/β titanium alloys and by Swift and Rodgers for stress-relief cracking of 2¼Cr-1Mo steels (Refs. 20, 61). In titanium alloys system, cracking occurs in the temperature regime of the $\beta \rightarrow \alpha$ phase transformation and Rath and coworkers have postulated that the stress associated with this transformation causes cracking. Similar to the present study, grain boundary α typically nucleates with the Burger's orientation relationship $(110)_\beta \parallel (0001)_\alpha$, $[111]_\beta \parallel [1120]_\alpha$, and is believed to generate significant local stresses (Ref. 20). While there is no general agreement on the mechanism or mechanisms of subsolidus cracking in titanium alloys, the precipitation-based mechanism of Rath et al. is generally consistent with the susceptibility of a wide range of model alloys (Ref. 20). Similarly, the research of Swift and Rodgers indicates that reheat cracking in 2¼Cr-1Mo steels occurs when partially coherent $\{(110)_\alpha \parallel (001)_{\text{Mo}_2\text{C}} \text{ and } [100]_\alpha \parallel [110]_{\text{Mo}_2\text{C}}\}$ Mo_2C carbides form. Resistance to cracking is reestablished when precipitates grow in size and are no longer able to impart coherency strains on the matrix (Ref. 61).

The correspondence of ductility loss to precipitation of a partially or fully coherent precipitates in other alloys helps validate the findings of the present study and indicates that DDC, strain-age cracking, reheat cracking, and observations of intermediate temperature ductility loss are often caused by precipitation-induced cracking. In alloys where precipitation of partially coherent or coherent precipitates with large misfit occurs at short times (e.g., A690, EN52, Astroloy and IN-100), the result is a weldability problem. In alloys where precipitation of the misfitting second phase is sluggish, ductility loss is often observed during hot tensile testing or deformation processing (e.g., X-750, Inconel 718, and Monel K-500). The key point is that ductility loss occurs in the time/temperature regime where the global stresses overlap with the local, precipitation-induced stresses. Welding-induced cracks are promoted by large precipitation-induced stresses, large global stresses (e.g., high weld constraint), and with increasing volume fraction of the detrimental second phase.

Conclusions

Ductility dip cracking in Ni-Cr alloys is likely a form of precipitation-induced cracking similar to intermediate temperature tensile ductility loss noted in several other nickel-based alloys, strain-age cracking in superalloys, subsolidus cracking in titanium alloys, and stress-relief cracking in ferritic steels. In Ni-(20–30 wt-%)Cr alloys, DDC is caused by the combination of macroscopic thermal and solidification stresses induced during welding and local stresses generated during grain boundary precipitation of partially coherent $(\text{Cr,Fe})_{23}\text{C}_6$ carbides. The strong correlation between the time/temperature dependence of DDC with precipitation, but not with grain boundary impurity segregation (e.g., sulfur) indicates that for the compositions tested, segregation is not a significant factor. Cracking can be mitigated by alloying to minimize grain boundary $(\text{Cr,Fe})_{23}\text{C}_6$ precipitation (e.g., by Nb and Ti additions), lessening the misfit between the matrix and these precipitates (lowering the Cr concentration), and by minimizing welding-induced stresses (e.g., by avoiding dissimilar metal welds). The alloying strategies outlined herein, offer promising avenues to improve the weldability of high-chromium nickel-alloy filler metals while maintaining the outstanding corrosion resistance required for many power generation applications of these materials.

Acknowledgments

The authors wish to thank Dr. Rick Noecker, Dr. Masashi Watanabe, and Prof. John DuPont of Lehigh University for their important contributions to this work. Additionally, at Lockheed Martin we gratefully acknowledge the assistance of Mr. Dominick Amedio, Dr. Cathy Jordan, Mr. Nathan Lewis, Dr. Reza Najafabadi, Mr. Paul Sander, and Dr. John Sutliff for their help in this research.

References

- Gorman, J. A. 2001. Corrosion problems in the nuclear industry and implications for the future in chemistry and electrochemistry of stress corrosion cracking. A symposium honoring the contributions of R. W. Staehle, TMS.
- Bamford, W., and Hall, J. 2003. A review of Alloy 600 cracking in operating nuclear plants: historical experience and future trends. *11th International Conference on Environmental Degradation of Materials in Nuclear Power Systems-Water Reactors*. Stevenson, Wash., NACE.
- Young, G. A., et al. 2005. The mechanism and modeling of intergranular stress corrosion cracking of nickel-chromium-iron alloys exposed to high purity water. *12th International Conference on Environmental Degradation of Materials in Nuclear Power Systems*. Salt Lake City, Utah, TMS.

- Young, G. A., and Capobianco, T. E. 2007. Development of a highly weldable and corrosion resistant Ni-Cr filler metal. *13th Conference on Environmental Degradation of Materials in Nuclear Power Systems*. Whistler, BC, Canada, CNS.
- Inconel® Alloy 690. 1980, Huntington Alloys.
- Jacko, R. J., Gold, R. E., and Kroes, A. 2006. Accelerated corrosion testing of Alloy 52M and Alloy 182 weldments. *11th International Conference on Environmental Degradation in Nuclear Power Systems - Water Reactors*. Stevenson, Wash., TMS.
- Nippes, E. F., Savage, W. F., and Grotke, G. 1957. Further studies of the hot-ductility of high-temperature alloys, Welding Research Council, New York, N.Y.
- Nissley, N. E., and Lippold, J. C. 2003. Development of the strain-to-fracture test. *Welding Journal* 82(12): 355-s to 364-s.
- Ramirez, A. J., and Lippold, J. C. 2004. High temperature behavior of Ni-base weld metal, Part I. ductility and microstructural characterization. *Mat. Sci. & Eng. A*, 2004. 380: 259–271.
- Ramirez, A. J., and Lippold, J. C. 2004. High temperature behavior of Ni-base weld metal, Part II. Insight into the mechanism for ductility dip cracking. *Mat. Sci. & Eng. A*, 380: 245–258.
- Capobianco, T. E., and Hanson, M. 2005. Auger spectroscopy results from ductility dip cracks opened under ultrahigh vacuum. *Proceedings of the 7th International Conference Trends in Welding Research*. Callaway Gardens, Ga., ASM International.
- Collins, M. G., Ramirez, A. J., and Lippold, J. C. 2003. An investigation of ductility dip cracking in nickel-based weld metals — Part 2. *Welding Journal* 82: 348-s to 354-s.
- Collins, M. G., Ramirez, A. J., and Lippold, J. C. 2004. An investigation of ductility-dip cracking in nickel-based weld metals — Part 3. *Welding Journal* 83: 39-s to 49-s.
- Inconel® Alloy X-750. 1998. Inco Alloys International, Huntington, W.Va. pp. 1–25.
- Inconel® Alloy 718. 1985, International Nickel Co., Inc.
- Dave, V. R., et al. 2004. Grain boundary character in Alloy 690 and ductility-dip cracking. *Welding Journal* 83: 1-s to 5-s.
- Weiss, B., Grotke, G. E., and Stickler, R. 1970. Physical metallurgy of hot ductility testing. *Welding Journal* 49: 471-s to 487-s.
- Rhines, F. N., and Wray, P. J. 1961. Investigation of the intermediate temperature ductility minimum in metals. *Trans ASM* 54: 17–128.
- Engineering Properties of Monel® Alloy K-500. 1965. International Nickel Co.
- Rath, B. B., et al. 1994. High Temperature Ductility Loss in Titanium Alloys — A Review, DE-AC04-94AL85000. 1994, Sandia National Laboratories.
- Damkroger, B. K., Edwards, G. R., and Rath, B. B. 1989. Investigation of subsolidus weld cracking in alpha-beta titanium alloys. *Welding Journal* 68: 290-s to 302-s.
- Hayduk, D., et al. 1986. Cracking susceptibility of Ti-6Al-2Nb-1Ta-0.8Mo as determined by the Varestraint test. *Welding Journal*, 65: 251-s to 260-s.
- Bowden, D. M., and Starke, E. A. 1984. The effect of microstructure and deformation

behavior on the hot ductility of Ti-6Al-2Nb-1Ta-0.8Mo. *Met. Trans A*, 15A: 1687-1698.

24. Noecker, F. F., and DuPont, J. N. 2005. Microstructural characterization and hot ductility of nickel based weldments. American Welding Society, Dallas, Tex.

25. Collins, M. G., and Lippold, J. C. 2003. An investigation of ductility dip cracking in nickel-based filler materials — Part 1. *Welding Journal* 82: 288-s to 295-s.

26. Yeniscavich, W. 1987. *Joining, in Super-alloys II*, C. T. Sims, N. S. Stoloff, and W. C. Hagel, editors. John Wiley & Sons: New York, N.Y., pp. 495-516.

27. Patriarca, P. 1967. Effects of minor elements on the weldability of high nickel alloys. Houston, Tex., Welding Research Council.

28. Yeniscavich, W., and Fox, C. W. 1967. Effects of minor elements on the weldability of Hastelloy® alloy X. *Effects of Minor Elements on the Weldability of High-Nickel Alloys*. Houston, Tex., Welding Research Council.

29. Canonico, D. A., et al. 1967. Effects of minor additions on weldability of Incoloy® 800. *Effects of Minor Elements on the Weldability of High-Nickel Alloys*. Houston, Tex., Welding Research Council.

30. *Welding, Brazing, and Soldering*. Online Edition 1993. *ASM Handbook*. Vol. 6.

31. Group, E., Sysweld. 2005.

32. *JMatPro* version 4.0. 2005, Sente Software: Guildford, UK.

33. Saunders, N., et al. 2003. Modeling of thermo-physical and physical properties relevant to solidification. *Advanced Solidification Processing X*, TMS.

34. Bale, C. W., et al. 2005. *FactSage*. Thermfact, Montreal, Canada.

35. *Medea* Version 2.1. 2005, Materials Design, Inc.

36. Mulford, R. A. 1983. Grain-boundary embrittlement of Ni and Ni alloys. *Materials Science and Technology — Embrittlement of Engineering Alloys*, C. L. Briant and S. K. Banerji, editors. Academic Press: New York. pp. 1-19.

37. Bruemmer, S. M., et al. 1983. Influence of sulfur, phosphorus, and antimony segregation on the intergranular hydrogen embrittlement of nickel. *Met. Trans. A*, 14A: 223-232.

38. Young, G. A., et al. 2003. An atomistic modeling study of alloying element, impurity element, and transmutation products on the cohesion of a nickel Σ5 {001}twist grain boundary. *11th Conference on Environmental Degradation of Materials in Nuclear Power Systems - Water Reactors*. Stevenson, Wash., ANS.

39. Edington, J. W. 1976. *Practical Electron Microscopy in Materials Science*, Hendon, Va., Tech Books.

40. Yonezawa, T., Yamaguchi, Y., and Iijima, Y. Electron micro-autoradiographic observation of tritium distribution on alloy X750. *Proceedings of the International Symposium on Plant Aging and Life Predictions of Corrodible Structures*. Sapporo, Japan.

41. Yeniscavich, W. 1966. A correlation of Ni-Cr-Fe alloy weld metal fissuring with hot ductility behavior. *Welding Journal* 45: 344-s to 356-s.

42. Mulford, R. A. 1983. Grain boundary segregation in Ni and binary Ni alloys doped with sulfur. *Met. Trans A.*, 14A: 865-870.

43. Jones, R. H., and Bruemmer, S. M. 1988. Environment-induced crack growth processes in nickel-base alloys, *Environment-Induced*

Cracking of Metals, R. P. Gangloff and M. B. Ives, editors, NACE. pp. 287-310.

44. Sims, C. T., Stoloff, N. S., and Hagel, W. C., eds. 1987. *Superalloys II*, John Wiley & Sons: New York, p. 615.

45. *Inconel Alloy 600*, SMC 027. 2000. Special Metals Corp., Huntington, W.Va., p. 19.

46. Marucco, A. 1994. Atomic ordering in the Ni-Cr-Fe system. *Mat. Sci. & Eng.*, A189: 267-276.

47. Lim, Y. S., et al. 2004. The effect of grain boundary misorientation on the intergranular M₂₃C₆ precipitation in thermally treated Alloy 690. *J. Nucl. Mat.*, 335: 108-114.

48. Norring, K., Stiller, K., and Nilsson, J. O. 1991. Grain boundary microstructure, chemistry, and IGSCC in alloy 600 and Alloy 690. *5th International Symposium on Environmental Degradation of Materials in Nuclear Power Systems - Water Reactors*. Monterey, Calif.

49. Hinnuber, J., and Rudiger, O. 1954. Chromium carbide in hard metal alloys. *Symposium on Powder Metallurgy*.

50. Johnson, W. C. 2000. Superficial stress and strain at coherent interfaces. *Acta Mat.*, 48: 433-444.

51. *Huntington Nickel Alloys*. 1968, International Nickel Co., Huntington, W.Va.

52. *Monel: Nickel-Copper Alloys*. 1969. International Nickel Co., Huntington, W.Va.

53. Dix, A. W., and Savage, W. F. 1973. Short time aging characteristics of Inconel X-750. *Welding Journal* 52: 135-s to 139-s, 144-s.

54. Kuo, K. 1953. The formation of Eta carbides. *Acta Met.*, 1: 301-304.

55. Prager, M., and Shira, C. S. 1968. Welding Research Council Bulletin 128.

56. Hughes, W. P., and Berry, T. F. 1967. A study of the strain-age cracking characteristics in welded Rene® 41 — Phase I. *Welding Journal* 46: 361-s to 370-s.

57. Berry, T. F., and Hughes, W. P. 1969. A study of the strain-age cracking characteristics in welded Rene® 41 — Phase II. *Welding Journal* 48: 505-s to 513-s.

58. Franklin, J. E., and Savage, W. F. 1974. Stress relaxation and strain-age cracking in Rene® 41 weldments. *Welding Journal* 53: 380-s to 387-s.

59. Messler, R.W., *Principles of Welding*. 1999, New York: John Wiley & Sons.

60. Schwenk, W., and Trabold, A. F. 1963. Weldability of Rene® 41. *Welding Journal* 42(10): 460-s to 465-s.

61. Swift, R. A., and Rodgers, H. C. 1973. Embrittlement of 2¼Cr-1Mo steel weld metal by postweld heat treatment. *Welding Journal* 52: 145-s to 153-s, 172-s.

62. Yakel, H. L. 1987. Atom distributions in tau carbide phases. *Acta Crystallographica*, B43: 230-238.

63. Sander, P. C. 2005. Lattice parameters of selected nickel-based alloys as determined by X-ray diffraction. G. A. Young, Schenectady, personal communication.

64. Kittel, C. 1996. *Introduction to Solid State Physics*. 7th ed., New York: John Wiley & Sons. p. 673.

An Important Event on Its Way?

Send information on upcoming events to the Welding Journal Dept., 550 NW LeJeune Rd., Miami, FL 33126. Items can also be sent via FAX to (305) 443-7404 or by e-mail to woodward@aws.org.

Dear Readers:

The *Welding Journal* encourages an exchange of ideas through letters to the editor. Please send your letters to the Welding Journal Dept., 550 NW LeJeune Rd., Miami, FL 33126. You can also reach us by FAX at (305) 443-7404 or by sending an e-mail to Kristin Campbell at kcampbell@aws.org.